Plasmonic Functional Assay Platform Determines the Therapeutic Profile of Cancer Cells

Arif E. Cetin,* Seda Nur Topkaya, Ziya Ata Yazici, and Ozden Yalcin-Ozuysal

Cite This: https://doi.org/10.1021/acssensors.3c00208

Read Online

ACCESS | Metrics & More | Article Recommendations

ABSTRACT: Functional assay platforms could identify the biophysical properties of cells and their therapeutic response to drug treatments. Despite their strong ability to assess cellular pathways, functional assays require large tissue samples, long-term cell culture, and bulk measurements. Even though such a drawback is still valid, these limitations did not hinder the interest in these platforms for their capacity to reveal drug susceptibility. Some of the limitations could be overcome with single-cell functional assays by identifying subpopulations using small sample volumes. Along this direction, in this article, we developed a high-throughput plasmonic functional assay platform to identify the growth profile of cells and their therapeutic profile under therapies using mass and growth rate statistics of individual cells. Our technology could determine populations' growth profiles using the growth rate data of multiple single cells of the same population. Evaluating spectral variations based on the plasmonic diffraction field intensity images in real time, we could simultaneously monitor the mass change for the cells within the field of view of a camera with the capacity of > ~500 cells/h scanning rate. Our technology could determine the therapeutic profile of cells under cancer drugs within few hours, while the classical techniques require days to show reduction in viability due to antitumor effects. The platform could reveal the heterogeneity within the therapeutic profile of populations and determine subpopulations showing resistance to drug therapies. As a proof-of-principle demonstration, we studied the growth profile of MCF-7 cells and their therapeutic behavior to standard-of-care drugs that have antitumor effects as shown in the literature, including difluoromethylornithine (DFMO), 5-fluorouracil (5-FU), paclitaxel (PTX), and doxorubicin (Dox). We successfully demonstrated the resistant behavior of an MCF-7 variant that could survive in the presence of DFMO. More importantly, we could precisely identify synergic and antagonistic effects of drug combinations based on the order of use in cancer therapy. Rapidly assessing the therapeutic profile of cancer cells, our plasmonic functional assay platform could be used to reveal personalized drug therapies for cancer patients.

**KEYWORDS:** plasmonics, cell growth, functional assays, diffraction field imaging, nanotechnology, nanohole arrays
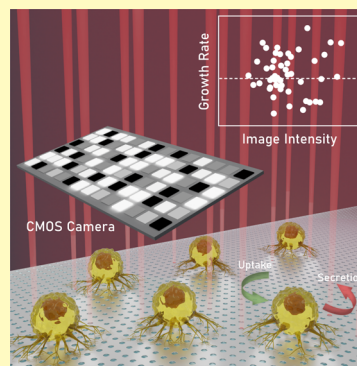
Thanks to the recent advancements in the treatment methods, mortality rates for many cancer types dramatically decreased.[1−5] However, some cancer types are still incurable due to the heterogeneity within the patient response, which induces a strong drug resistance[1,6−9] and relapse.[10−12] Therefore, developing methods to effectively target these subpopulations is of great importance. Currently, many treatment methods determine therapeutic profile based on the presence or absence of genetic or physiological markers.[13] However, there are two important factors that significantly affect the success of these methods, e.g., (i) insufficient numbers of validated biomarkers[14] and (ii) inability to assess the response of resistant subpopulations.[15−17] Biomarkers are usually developed by the analysis of bulk omics data, which might fail to represent intratumoral heterogeneity. Subpopulations and the evolution of subclones in response to drug treatments within the same tumor might result in differences in the treatment response and could lead to drug resistance. Thus, functional assessment of subpopulations' behavior is essential to estimate the drug response of

heterogeneous tumors.[18,19] Furthermore, existing biomarkers are developed by monitoring large numbers of patients. However, this methodology complicates the whole treatment process for relapse that occurs for the patients undergoing a therapy determined with the use of biomarkers. On the other hand, sequencing could resolve heterogeneity at the cellular level, while it still requires validated biomarkers and its throughput is low.[20] In contrast to these methods, functional assays could reveal drug sensitivity through phenotypic factors thanks to the direct use of patients' own cells.[16] In this method, the therapeutic response of cells to drug treatments is determined with functional biomarkers, which are indicative
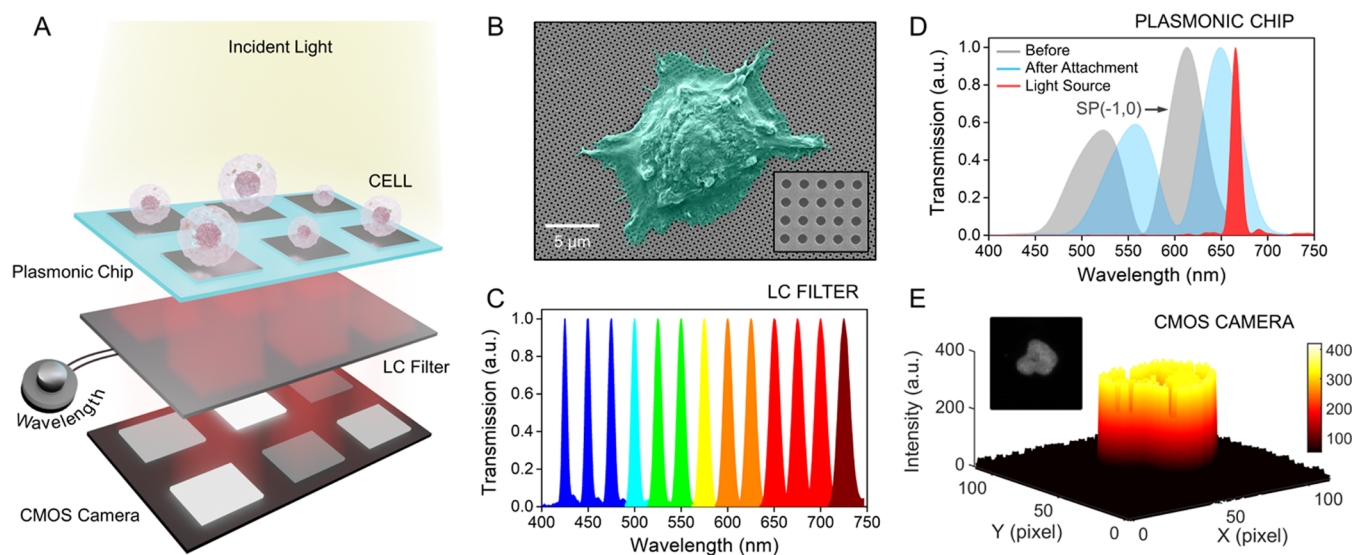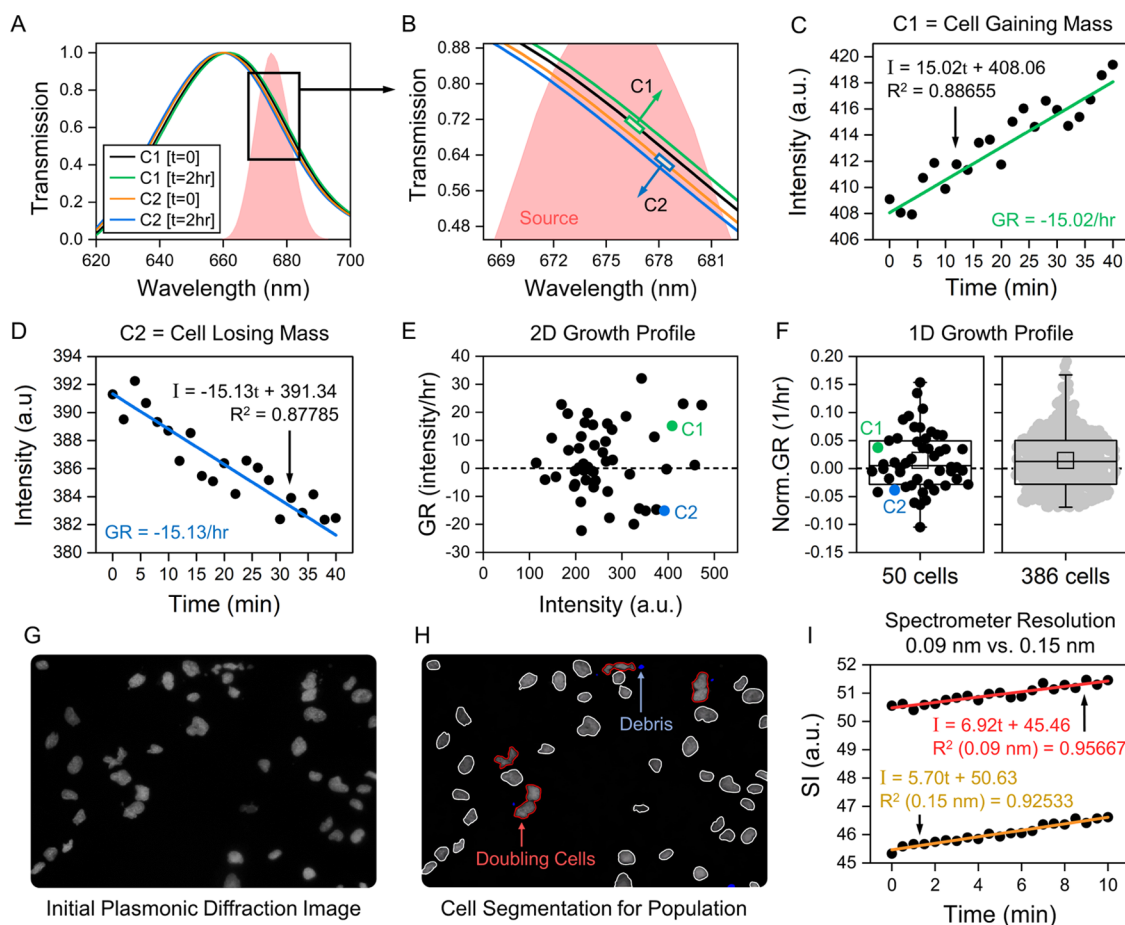
Figure 1. Components of the plasmonic functional assay platform. (A) Schematic illustration of the plasmonic functional assay platform determining growth profile of cells to assess their therapeutic response. In the schematics, the square areas on the plasmonic chip highlight the sensor locations containing individual cells. These sensor locations were drawn as squares in order to clearly explain the concept of our imaging-based technique. In reality, nanoholes cover the whole plasmonic chip surface, and in the CMOS camera, high-contrast cell images are observed instead of intensity images in square format. (B) MCF-7 cell adhered on the plasmonic chip surface textured with subwavelength nanohole arrays. (C) Transmission spectra of the light sources created with the tunable LC bandpass filter with 10 nm bandwidth. (D) Transmission response of the nanohole arrays under cell medium before (gray curve) and after (blue curve) the attachment of an MCF-7 cell on metal surface. The light source used for this scenario to create diffraction field images is highlighted with the red curve. (E) High-contrast diffraction field image of an MCF-7 cell on the plasmonic chip surface.

parameters of intra- or extracellular dynamics.[21] Direct measurement and quantification of disease-related parameters could guide to make accurate decisions for patient care. However, an in vitro functional assay platform routinely used in the clinic for the identification of therapeutic profile is not available yet. Furthermore, the success of functional assays is limited by various factors, e.g., the need for large tissue samples, operating based on long-term cell cultures or population-based bulky measurements, and requiring ex vivo primary cell proliferation, which is absent in many cases. Despite these challenges, functional assays have a great potential in monitoring the therapeutic profile of patients and assessing the response of subpopulations to specify personalized cancer therapy.[22,23] As opposed to the bulk measurements targeting population growth, determining population behavior in single-cell precision over a short time interval upon an external stimulus could provide more accurate information related to the active ingredients. In this respect, accessing single-cell growth could distinguish the cellular repose of minor groups possessing distinct biochemical or biophysical properties compared to the population. As one approach, single-cell growth could be determined based on cell volume, where 2-dimensional microscopic cell images are used. Unfortunately, the mathematical assumptions for cell height could be only applicable to few types of cells, which could even vary within the same population.[24] Quantitative phase microscopy is another methodology that determines the dry mass of cells, which could be also used for limited number of cell types.[25] Furthermore, suspended mechanical resonators could swiftly access single-cell mass with high precision, while this technique requires cells in suspension.[16]

In order to address these drawbacks, we recently introduced a plasmonic functional assay platform determining the distinct behavior of subpopulations via accessing the growth profile of

single cells.[26] Employing a highly sensitive plasmonic chip and a spectrometer system composed of simultaneously operating multiple spectrometers, the platform could monitor the uptake or secretion of molecules in real time, which alters the total cell mass. Using our platform, we could successfully assess different intracellular metabolisms that are critical for proliferation. We also determined the therapeutic profile of cells and heterogeneity within populations by categorizing them as sensitive and resistant under certain therapeutic agents. Despite its highly sensitive nature that could successfully assess the biophysical properties and therapeutic profiles of cells, the system throughput of this platform is low since each sensor location containing an individual cell in the plasmonic chip needs to be monitored sequentially with the spectrometer system rather than simultaneously.

Herein, we improved the spectral read-out of such configuration for a dramatic increase in the system throughput by replacing the spectrometer system with a CMOS (complementary metal–oxide–semiconductor) camera. Figure 1A shows the schematics of the high-throughput and plasmonic functional assay platform. The system employs a plasmonic chip, where the cells are seeded for growth-profiling measurements. The plasmonic chip is based on periodic nanohole arrays fabricated through a 120 nm thick aluminum film. The aluminum surface was coated with a silicon dioxide film, which stimulates cell adhesion and eliminates metal oxidation to maintain plasmonic properties.[26] Thickness of this coating is only 2 nm, i.e., it does not decrease the sensitivity of the plasmonic chip to the refractive index variations since the film does not overlap with the perpendicular component of the surface plasmon (SP) waves.[27] In the array, the hole diameter is 200 nm and the periodicity is 400 nm. Nanohole features were realized with a high-resolution fabrication technique, which yields uniformity over a large area (see the Experimental

Figure 2. Working principle of the plasmonic functional assay platform. (A) Transmission resonances supported by the nanohole arrays in the cell media, where the sensing surface is seeded with a cell gaining [C1] and losing [C2] mass. (B) Transmission resonances zoomed within the spectral region highlighted with a black box in (A). For C1, transmission resonance shifts toward longer wavelengths after 2 h (black curve to green curve). For C2, transmission resonance shifts toward shorter wavelengths after 2 h (orange curve to blue curve). In the figure, spectral behavior of the light source is highlighted in red. (C, D) Change in the diffraction field intensity (black dots) with time, where growth rate (GR) is calculated by using the slope of the linear fits for cells C1 (green line) and C2 (blue line). (E) GR vs intensity data for single cells (black dots), presenting the 2-dimensional growth profile of the population. GR values calculated for C1 and C2 are highlighted with green and blue dots, respectively. (F) Left: 1-dimensional growth profile calculated by normalizing GR of each cell by the intensity value of the same cell. Normalized GR values calculated for C1 and C2 are highlighted with green and blue dots, respectively. Number of MCF-7 cells used in the growth profile calculations is 50. Right: The same normalized growth profile calculated from 386 cells. The box plot represents the interquartile range, and the white square is the average value of GR data. (G) Plasmonic diffraction field image of MCF-7 cells seeded on the plasmonic chip surface. (H) Cell segmentation algorithm, revealing single cells (white), doubling or aggregating cells (red), and cell debris (blue). (I) SI (spectral integral) values calculated for two spectrometer-based platforms for two mass-gaining cells. The linear fits to the SI data for 0.09 nm (red line) and 0.15 nm (orange) spectral resolution yield different R-squared values due to the spectral variances associated with the spectral resolution.

Section for the fabrication of the plasmonic chips). The structural uniformity supports identical plasmonic properties across the entire plasmonic chip surface, i.e., cells on the same chip could be evaluated fairly in the growth-profiling measurements. In the optical setup, a broadband white LED (light-emitting diode) light passes through the plasmonic chip and reaches a tunable liquid crystal (LC) bandpass filter (Thorlabs Kurios). The transmitted light from the LC filter reaches the CMOS sensor (Zeiss Axiocam), forming the plasmonic diffraction field images. An incubator (PeCon) integrated into an inverted microscope (Zeiss Axio) was used to maintain CO_2, temperature, and humidity levels required for cell culture. Figure 1B shows the scanning electron microscopy (SEM) image of an MCF-7 human breast cancer cell on the plasmonic chip surface (see the Experimental Section for the preparation of the cell culture). In our technique, cells were incubated on the surface of the plasmonic chip 24 h prior to

each test in order to eliminate the effect of cell adhesion phases.[26] The silicon dioxide film on top of the plasmonic chip ensures strong cell adhesion thanks to its porous and rough surface, eliminating the need for surface modification, e.g., the cells were simply seeded on the plasmonic chip surface and incubated for 24 h. Previously, we also showed that cell migration on the sensing surface after strong cell adhesion (occurred at cell adhesion phase III) does not alter the spectral calculations for the individual cell growth profiling.[26] Figure 1C shows the spectra of the light sources created with the LC filter at different wavelengths within the visible range. Here, the center wavelength could be tuned from 420 nm to 730 nm with 1 nm incremental step size, while the bandwidth is as narrow as 10 nm. Previously, we used this imaging methodology to reconstruct plasmonic modes, where we could demonstrate similar refractive index sensitivities with the classical spectrometer-based read-out schemes.[28]

In the plasmonic chip, the aluminum film was fabricated on a glass substrate that is coated with a silicon nitride interlayer. This interlayer between the metal film and the glass layer eliminates the undesired SP modes excited between metal/glass interface, which yields a well-defined transmission resonance.[29] The transmission resonance is due to the SP(-1,0) mode excited at the top aluminum surface, which employs the unique integration of localized and propagating SPs. This mode is associated with large local electromagnetic fields, extending extensively within the adjacent medium which makes it highly accessible, i.e., it yields high sensitivities to the refractive index changes.[30] The growth-profiling measurements under the incubator conditions were performed on cells seeded on the surface of the plasmonic chip immersed in cell media, ensuring their activity and proliferation. Figure 1D shows the transmission spectrum of the nanohole arrays under cell medium (gray curve), where the SP(-1,0) mode is indicated with an arrow. The transmission resonance shifted by ∼34.65 nm (blue curve) after the attachment of the cell on the chip sensor (24 h seeding time). LC filter was tuned to a wavelength ∼16.12 nm longer (red curve) than the transmission resonance for the cell attachment (blue curve). Figure 1E shows the CMOS camera image of an MCF-7 cell on the plasmonic chip surface. Here, the cell-free chip surface is black since the transmission resonance under the cell medium does not spectrally overlap with the LC filter. On the other hand, the sensor region covered with the cell has high intensity due to the better overlap between SP(-1,0) mode and the filter response, which allows a large number of photons reaching the CMOS imager. Therefore, by precisely positioning the bandpass filter with a narrow bandwidth, we could create high contrast between the sensor location and the background in the plasmonic diffraction field images.

■ MATERIALS AND METHODS

Working Principle of the Plasmonic Functional Assay Platform. In general, the net biomass of cells increases by accumulation when the molecular uptake exceeds secretion. On the other hand, cells lose mass when the secretion is higher. Figure 2A shows the spectral variations within the transmission resonance based on these two scenarios, where we evaluated two cells, one of which gains (C1) and loses (C2) mass for 2 h. Zooming to a smaller spectral window (Figure 2B), the transmission resonance initially at ∼660.9 nm (black curve) shifted toward longer wavelengths by ∼0.6 nm (green curve) due to the mass gain for cell C1. On the other hand, the transmission resonance initially at ∼660.1 nm (orange curve) shifted toward shorter wavelengths by ∼0.7 nm (blue curve) due to the mass loss for cell C2. Our fabrication technique ensures an identical transmission response throughout the plasmonic chip. Therefore, the difference between the initial position of the transmission resonances (black curve vs orange curve) is the mass difference between cells C1 and C2.[26] The small spectral variations within the transmission resonance are due to the minute mass accumulation rate, e.g., ∼pg/h,[16,17] which requires a highly sensitive platform that could differentiate minute refractive index changes. Using our plasmonic diffraction-imaging technique, we recently demonstrated the detection of protein molecules with sub-1 ng/mL detection limit.[31] Considering the transmission resonance with a Lorentzian shape and the sub-1 nm spectral variations within its spectral position in a 2-h-long measurement, the light source was positioned at 675 nm (red curve in Figure 2A,B). This methodology ensures that the transmission maximum always positions at wavelengths shorter than the light source during the growth-profiling tests, which eliminates the effect of Lorentzian shape of the transmission resonance on the growth rate calculations.[30]

Mass accumulation by a cell on the plasmonic chip surface increases the effective refractive index, shifting the transmission resonance toward longer wavelengths. This red shift makes the transmission resonance overlap better with the light source, i.e., it allows more photons to reach the CMOS imager, which increases the diffraction field intensities. In contrast, mass loss decreases the intensity due to the increase in the spectral mismatch between transmission resonance and the light source. As we previously showed, the transmission resonance supported by the nanohole arrays exhibits a consistent red or blue shift within 2 h, i.e., cellular behaviors could be evaluated in shorter durations.[26] Thus, we monitored these behaviors with our imaging-based technology over the course of 40 minutes. Figure 2C,D shows the real-time change in the diffraction field intensity for two different cells. In our technique, diffraction field intensity represents the cell mass, and the rate of mass change is analogous to growth rate (GR), which is calculated from the slope of the linear fit to the intensity vs time data. Here, the positive GR value (green line) is directly related to mass accumulation over time, while mass loss yields a negative GR value (blue line). Mapping GR vs intensity data, we generated a 2-dimensional growth profile for the population in single-cell resolution (Figure 2E). In this figure, intensity values on the x-axis are the initial intensity values determined in the beginning of the tests for each cell (in other words, the mass of each cell at t = 0). Here, the growth profile data demonstrates the heterogeneity both in mass and growth rate, e.g., large or small masses, and positive or negative growth rates. In the same figure, GR vs intensity data corresponding to the cells C1 and C2 are denoted with green and blue dots, respectively. Normalizing GR of each cell with the mass (in other words, intensity) of the same cell, we determined the 1-dimensional growth profile for the population (Figure 2F, left). Following this methodology, we could eliminate the cell cycle- and size-dependent effects, characterizing mass as a proxy for cell cycle phases.[32] Therefore, we used normalized GR values for growth-profiling calculations throughout the article. In the same figure, the normalized GR values corresponding to cells C1 and C2 are denoted with green and blue dots, respectively.

In order to have accurate population data, we conducted a cell segmentation algorithm that could assign single cells, and eliminates cell debris as well as doubling (or aggregating, clustering) cells from the calculations. For each population study, we used 50 cells randomly chosen in the CMOS active area. Prior to the segmentation process, images were pre-processed with color space change and noise removal steps. In our imaging-based technique, we used a monochromatic CMOS camera, i.e., the algorithm is based on monitoring the intensity variation in grayscale. In order to prevent false detection of cell boundaries and eliminate unnecessary defects, we smoothed the image with a Gaussian filter (5×5, $\sigma = 1$) that suppresses noises. In the diffraction images, pixels covered with cells have higher intensities compared to the background, i.e., we could use intensity differences to extract cells from the background. In the cell extraction algorithm, we employed an adaptive thresholding method, e.g., Otsu's method.[33] In this method, images were iteratively thresholded by different intensity values, and the threshold values resulting in the minimum intraclass intensity variance were returned. The images were then thresholded with the returned value, and a binary mask was obtained where the objects have white color. Potential cells were separated from the background with white color. In order to detect the white pixel clusters on the images, we first applied image contouring to determine boundaries. We could determine the perimeter and the area of each potential cell pixel-by-pixel from the contours. The values were then averaged, and the standard deviation values were separately acquired for perimeter and area values. In order to eliminate doubling or aggregating (clustering) cells and cell debris from our calculations, it is critical to determine anomalies in the images. Here, we used a definition, where we compared each cell candidate. The detected objects that have smaller areas compared to [*average area − standard deviation*] were classified as debris, while the objects that have larger perimeters compared to [*average perimeter + standard deviation*] were classified as doubling cells. The remaining objects were assigned to the cell class. Figure 2G shows a plasmonic diffraction field image of

D
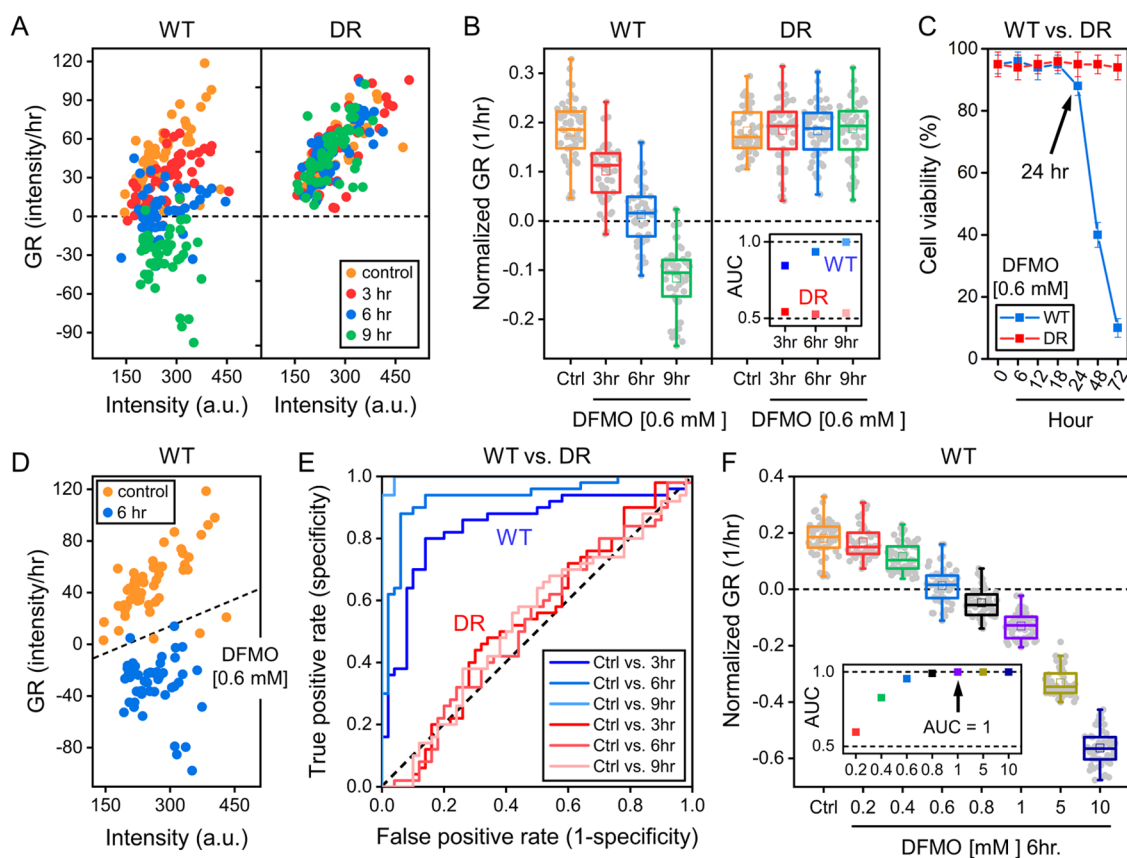
Figure 3. Plasmonic platform reveals therapeutic heterogeneity. (A) GR vs intensity data for WT and DR cells under different DFMO exposure durations (DFMO concentration is 0.6 mM). (B) Normalized GR profile for WT and DR cells for different DFMO exposure duration. (C) Cell viability under different DFMO exposure durations (DFMO concentration is 0.6 mM), WT/DR: blue/red dots. The arrow highlights the time when a reduction starts to appear within the viability of WT cells. Squares are the mean values, and the error bars are double the standard deviation of five independent experiments. (D) GR vs intensity data for WT control cells (blue dots) and WT cells under DFMO exposure (0.6 mM and 6 h) separated by the orthogonal vector overlay that designates a threshold determined from LDA (dashed line). In (A) and (D), the data corresponding to control WT cells (orange dots) and WT cells under 0.6 mM and 6 h. DFMO exposure (blue dots) are the shared data. (E) ROC curves for control and DFMO-treated WT (blue lines) and DR (red lines) cells at different exposure duration (3, 6, 9 h.) The inset in (B) shows the AUC values calculated from ROC analyses for each exposure duration. (F) Normalized GR profile of WT cells under different DFMO concentrations from 0.2 to 10 mM (exposure duration is 6 h). The inset in (F) shows the AUC values calculated for different DFMO concentrations. The arrow indicates the DFMO concentration, where AUC converges to 1. In (B) and (F), the data corresponding to control WT cells (orange boxes) and WT cells under 0.6 mM and 6 h DFMO exposure (blue boxes) are the shared data. In the normalized GR profiles, boxes represent the interquartile range, and white squares are the average value of GR data. The number of MCF-7 cells used in the growth profile calculations is 50.

MCF-7 cells adhered on the chip surface. Figure 2H shows the processed image demonstrating single cells (white), doubling or aggregating (clustering) cells (red), and debris (blue). Finally, we averaged the total diffraction field intensity with the number of pixels in the detected area to determine the mass of each cell.

For a detection scheme based on plasmonic diffraction field images, spectral resolution is the most critical parameter to detect minute changes occurring in a short period. As we have shown earlier, the spectral resolution of our technique is defined by the bandwidth of the light source, e.g., decreasing the bandwidth strengthens the spectral resolution.[28] For our tunable LC filter, the sharpest light source has a bandwidth of 10 nm, which yields a spectral resolution above 0.15 nm.[28] Spectral resolution determines the variance between each spectral data associated with the dynamic mass information. Here, we compared our platform's ability to access the growth rate of cells with two spectrometer-based setups with high spectral resolution, e.g., 0.09 and 0.15 nm (see the Experimental Section for the details of the spectrometer-based measurement setups). In order to determine the spectral variations due to the minute mass changes, we utilized a spectral integral method, where we considered the collective wavelength shifts within the transmission response of the nanohole arrays (see the Experimental Section for the spectral postprocessing

technique). Figure 2I shows the variations within the spectral integral (SI) values (analogous to the diffraction field intensity values in the imaging-based technique) due to two mass-gaining cells. Here, the R-squared values for the linear fits to the experimental data are compared for 0.09 nm (red line) and 0.15 nm (orange line) spectral resolutions. R-squared is the statistical measure, which demonstrates the accuracy of the fitted regression line, e.g., higher the R-squared, the better the model fits to the experimental data. R-squared is between 0 and 1, where R-squared = 1 refers to the perfect fit. As shown in Figure 2I, the spectrometer-based system with 0.09 nm resolution yields a higher R-squared value compared to the one with 0.15 nm resolution, which is due to the smaller variations within the raw data for the higher spectral resolution. In contrast to these highly sensitive spectrometer-based platforms, our regression line possesses a relatively lower R-squared value, which is due to the higher variances observed within the diffraction field images related to the lower spectral resolution of our plasmonic imaging technique. In order to compensate this drawback, we increased the test duration from 10 minutes (the duration used for the spectrometer-based configuration[26]) to 40 min, which increases the duration between each data point allowing larger shifts (due to larger mass changes) within the transmission resonance. This ensures distinguishable intensity differ-

ences between each measurement in the presence of a relatively lower spectral resolution. Even though the test duration increases with the use of an imaging-based scheme, the system throughput is still dramatically improved by simultaneously evaluating cells on the plasmonic chip surface (e.g., for 50 cells, the measurement time is still 40 min). On the other hand, for a spectrometer-based configuration, test duration is determined by the number of cells used in the growth rate analyses (e.g., for 50 cells, the measurement time is $50 \times 10 = 500$ min).

More importantly, employing a CMOS camera for tracking the plasmonic variations also provides the ability to monitor all cells within the CMOS camera's field of view for growth profile calculations. Under a 20× objective lens, our camera has $\sim 0.42 \times \sim 0.62$ mm field of view. Figure 2F (right) shows the 1-dimensional growth profile of MCF-7 cells determined from n = 386 cells, which exhibits a similar trend with the one determined from $n = 50$ cells, e.g., the mean normalized GR values are 0.0142 ($n = 50$) vs 0.0144 ($n = 386$). In order to compare the growth profile of cells belonging to the same population with different sample sizes, we used Welch's t-test, where significance level $\alpha = 5\%$. Here, α is between 0 and 1, i.e., for $p > 0.05$, two data sets do not show significant differences. Here, we determined p(50 cells vs 386 cells) = 0.9831, demonstrating their excellent overlap. Therefore, we used $n = 50$ cells throughout the manuscript for data presentation clarity (box plot + data). Our technique yields a capacity of $> \sim 500$ cells/h scanning rate. Therefore, combined with a motorized translation stage that allows imaging different locations of the plasmonic chip surface, thousands of cells could be evaluated within few h. As our methodology requires spectral measurements performed under an aqueous environment, external effects, e.g., water evaporation, do not alter the overall cell mass.

■ RESULTS AND DISCUSSION

Plasmonic Functional Assay Platform Determines Heterogeneity in Therapeutic Profile. In order to show the ability of our functional assay platform to identify heterogeneity in the therapeutic profile of cancer cells, we studied the response of MCF-7 cells to difluoromethylornithine (DFMO), which shows antitumor effects on this cell line.[34] Polyamine metabolism is critical for cell growth, which is regulated by ornithine decarboxylase (ODC), an enzyme required for polyamine synthesis.[35,36] ODC activity is high for cancer cells, and DFMO is the irreversible inhibitor of ODC.[37] Inhibiting ODC activity, in other words, inhibiting the polyamine synthesis leads to an antigrowth effect, e.g., increasing apoptosis or decreasing tumor invasion.[34,38] Here, we studied the effect of DFMO on the growth profile of MCF-7 cells, and their DFMO-resistant (DR) variants. DR cells were prepared by gradually treating MCF-7 cells to different DFMO concentrations (see the Experimental Section for the preparation of DR cells).[39]

Figure 3A shows the GR vs intensity data for WT and DR cells under 0.6 mM DFMO for 3, 6, and 9 h treatment duration. For each test, the normal cell media were replaced with the media containing DFMO. Here, treating WT cells with DFMO for only 3 h significantly reduces GR, and the reduction in GR is more pronounced for longer DFMO exposure. On the other hand, DR cells maintain normal growth and show no significant variations in their growth profile, which demonstrates their resistant behavior under an antitumor agent. Similar behavior could be also observed in the normalized GR profile (Figure 3B), e.g., the antigrowth effect of DFMO is stronger for longer drug exposure. For example, the mean normalized GR values for WT cells are 0.1805 (control), 0.1011 (3 h), 0.0131 (6 h), and −0.1165 (9 h), while for DR cells, 0.1826 (control), 0.1841 (3 h), 0.1830

(6 h) and 0.1871 (9 h). In comparison to our plasmonic functional assay platform, bulk cell viability tests by trypan blue for WT cells (blue dots in Figure 3C) require 24 h DFMO exposure for a meaningful reduction in the GR profile. This result shows that the reduction in GR could reveal the antitumor effect of DFMO much faster compared to the loss of cell viability.[17] On the other hand, DR cells (red dots in Figure 3C) show negligible variations in viability during the DFMO exposure. In order to compare the therapeutic profile of cells under different conditions, we used different statistical methods. Here, we first performed Welch's t-test. For the normalized GR data, we compared different DFMO exposure duration with the control group, where p-values were Bonferroni corrected. Increasing exposure duration made GR more negative, and p-values dramatically decreased, e.g., p(3 h) = 6.9005×10^{-9}, p(6 h) = 3.3225×10^{-28} and p(9 h) = 6.2016×10^{-40}. On the other hand, for DR cells, negligible differences were observed under different DFMO exposure durations due to their resistant behavior, e.g., p(3 h) = 0.8954, p(6 h) = 0.9708 and p(9 h) = 0.7035.

To show the robustness of our platform for cell classification based on their therapeutic profile, we performed linear discriminate analysis (LDA) and receiver-operating characteristics (ROC) on MCF-7 cells for different exposure duration. LDA projects the 2-dimensional GR vs intensity data onto a single axis, which best differentiates the two cell lines, and defines a classification threshold. Figure 3D shows the growth profile of WT control cells (orange dots) and WT cells exposed to 0.6 mM DFMO for 6 h (blue dots), where the LDA curve (dashed black line) separates the two groups. Following, we performed ROC analyses and calculated under the curve (AUC) providing a metric for classifying each cell as sensitive or resistant to an agent, where AUC = 0.5/1 is a random/ perfect classifier.[17,40] Figure 3E shows the ROC curves for WT (blue lines) and DR (red lines) cells for different DFMO exposure duration. Figure 3B (inset) shows the AUC values calculated from the ROC analyses. For different DFMO exposure duration, AUC for DR cells is ~ 0.5 (red dots), e.g., DFMO-treated DR cells are indistinguishable from untreated DR cells. On the other hand, ROC analyses reveal an excellent resolution between treated and untreated WT cells, e.g., AUC converges to 1 for longer DFMO exposure (blue dots). These findings confirmed that our plasmonic functional assay platform could selectively identify the heterogeneity in the therapeutic profile of cells for drug treatments.

In addition to the drug exposure duration, we investigated the discrimination of growth profiles between treated and untreated cells for a wide range of DFMO concentrations, e.g., 0.2 to 10 mM under 6 h exposure (Figure 3F). Here, we observed a larger reduction in GR profile at higher DFMO concentrations, e.g., the mean normalized GR value for control, 0.1805 dropped to 0.1682 (0.2 mM), 0.1158 (0.4 mM), 0.0131 (0.6 mM), −0.0479 (0.8 mM), −0.1302 (1 mM), −0.3317 (5 mM) and −0.5634 (10 mM). Welch's t-test performed between the control and treatment groups also shows the greater reduction in GR profile with DFMO concentration, e.g., p(0.2 mM) = 0.3411, p(0.4 mM) = 3.1683×10^{-7}, p(0.6 mM) = 3.3225×10^{-28}, p(0.8 mM) = 1.7658×10^{-35}, p(1 mM) = 6.5804×10^{-48}, p(5 mM) = 3.1739×10^{-66} and p(10 mM) = 4.6480×10^{-78}. ROC analysis exhibits a similar trend, i.e., AUC rapidly increases with concentration and converges to 1 at DFMO = 1 mM (Figure 3F, inset).

F
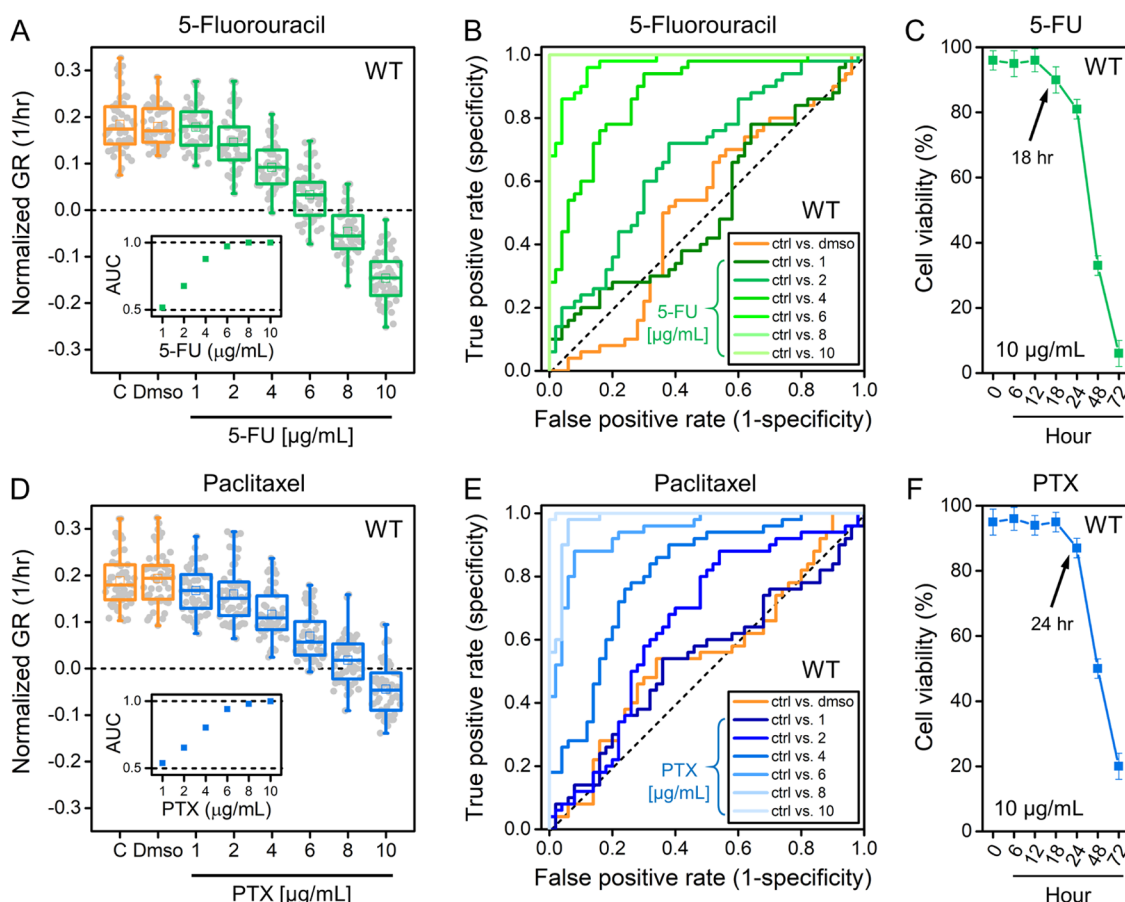
Figure 4. Plasmonic platform determines the therapeutic profile to single-drug therapies. Normalized GR profile of WT cells under different concentrations of (A) 5-FU and (D) PTX from 1 to 10 μg/mL (treatment duration, 6 h). Boxes represent the interquartile range, and white squares are the average value of GR data. Number of MCF-7 cells used in the growth profile calculations is 50. Control/DMSO: orange, 5-FU/PTX: green/blue. ROC curves for the untreated and treated WT cells for different (B) 5-FU and (E) PTX concentrations. The insets in (A) and (D) show the AUC values calculated for different drug concentrations. Cell viability under different (C) 5-FU and (F) PTX exposure duration (drug concentration is 10 μg/mL). The arrows highlight the time when a reduction starts to appear within the viability. For viability tests, squares are the mean values, and the error bars are double the standard deviation of five independent experiments.

Functional Assay Platform Defines Response to Single-Drug SOC Therapies. In order to show the ability of our plasmonic functional assay platform to define response to standard-of-care (SOC) drugs, we explored the growth profile of MCF-7 cells under a wide range of SOC single agents and their combinations. We first evaluated the response of MCF-7 cells to 5-Fluorouracil (5-FU), which is a cycle-specific cytotoxic chemotherapeutic agent used in the clinic to treat cancer. 5-FU has been used in the treatment of breast cancer since the 1950s.[41] Figure 4A shows the normalized GR profile of WT cells under different 5-FU concentrations, e.g., between 1 and 10 μg/mL (Treatment duration is 6 h). Here, greater reduction in GR for higher concentrations allows better discrimination between treated and untreated populations. For example, the mean normalized GR values were calculated as 0.1843 (control), 0.1796 (DMSO), 0.1779 (1 μg/mL), 0.1455 (2 μg/mL), 0.0918 (4 μg/mL), 0.0325 (6 μg/mL), -0.0460 (8 μg/mL) and -0.1466 (10 μg/mL). Welch's t-test applied between control and the treatment groups also exhibits a similar trend in GR profile, e.g., p(DMSO) = 0.6592, p(1 μg/mL) = 0.5677, p(2 μg/mL) = 0.0020, p(4 μg/mL) = 9.1031 $\times$ 10^{-13}, p(6 μg/mL) = 6.4107 $\times$ 10^{-23}, p(8 μg/mL) = 2.2302 $\times$ 10^{-36} and p(10 μg/mL) = 4.6297 $\times$ 10^{-49}. ROC analysis (Figure 4B) comparing control and the treatment groups

shows that AUC rapidly increases with concentration and converges to 1 at 8 μg/mL 5-FU (Figure 4A, inset). As an additional note, 5-FU was dissolved in dimethyl sulfoxide (DMSO). Normalized GR data (orange box in Figure 4A) shows that DMSO does not vary the growth profile of cells. Here, the corresponding ROC analysis between untreated WT cells and WT cells under DMSO yields a random classifier, e.g., AUC = ∼0.5 (orange line in Figure 4B).

As another SOC agent, we studied the response of MCF-7 cells to Paclitaxel (PTX), which is a chemotherapeutic agent used in the clinic to treat different cancer types including breast cancer.[42] Figure 4D shows the normalized GR profile of WT cells under different PTX concentrations, e.g., between 1 and 10 μg/mL (Treatment duration is 6 h). Here, higher susceptibility of WT cells to PTX therapy with larger concentrations yields greater reduction in GR, e.g., the mean normalized GR values were calculated as 0.1885 (control), 0.1934 (DMSO), 0.1672 (1 μg/mL), 0.16 (2 μg/mL), 0.1165 (4 μg/mL), 0.0693 (6 μg/mL), 0.0179 (8 μg/mL) and -0.0444 (10 μg/mL). A similar behavior could be observed with Welch's t-test, e.g., p(DMSO) = 0.6604, p(1 μg/mL) = 0.0448, p(2 μg/mL) = 0.0173, p(4 μg/mL) = 1.9463 $\times$ 10^{-9}, p(6 μg/mL) = 5.3485 $\times$ 10^{-19}, p(8 μg/mL) = 6.2697 $\times$ 10^{-29} and p(10 μg/mL) = 1.6188 $\times$ 10^{-38}. ROC analysis (Figure 4E)
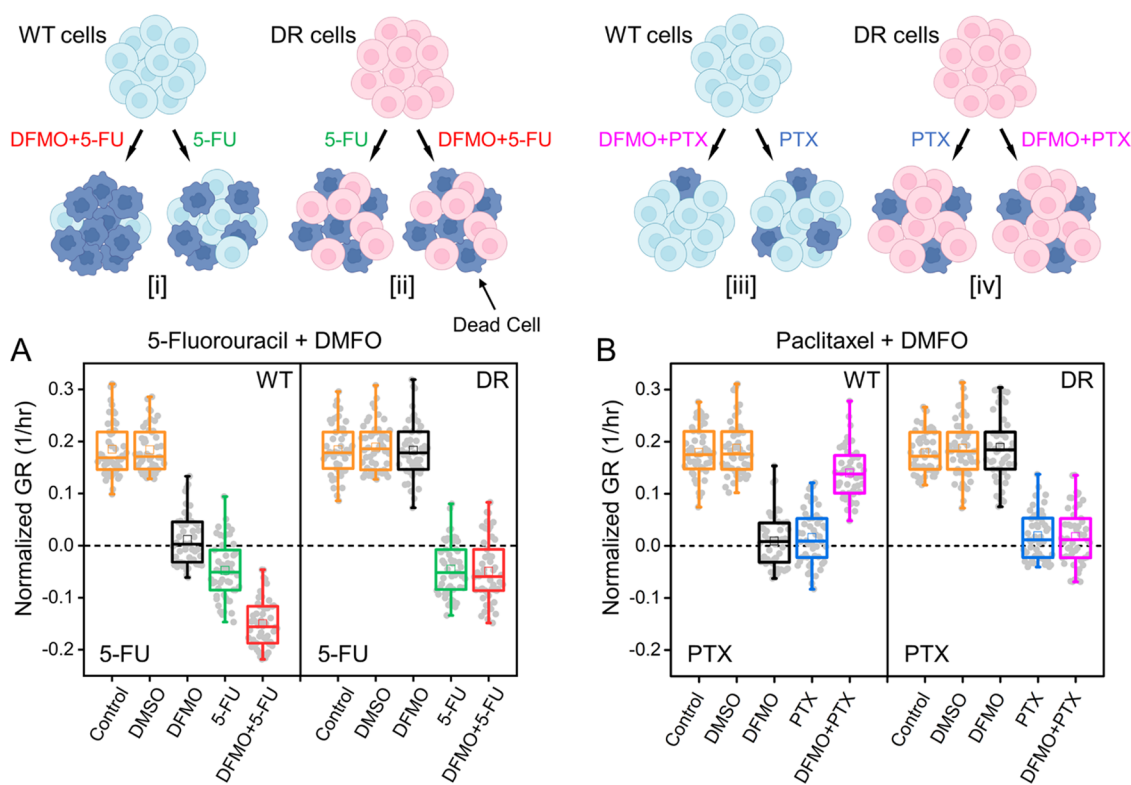
Figure 5. Plasmonic platform determines DFMO's role in different drug combinations. Schematics illustrates four cases: [i] WT cells are sensitive to DFMO and 5-FU, i.e., the viability of WT cells decreases with single 5-FU treatment, and the reduction in viability is more pronounced with the addition of DFMO. [ii] DR cells are resistant to DFMO, and sensitive to 5-FU, i.e., the reduction in viability for 5-FU and DFMO+5-FU is similar. [iii] WT cells are sensitive to PTX, and DFMO could reverse the cytotoxic effect of PTX, i.e., PTX therapy reduces the viability, while the viability under DFMO+PTX is higher compared to single PTX therapy. [iv] DR cells are sensitive to PTX, and their DFMO resistance inhibits the reversal of the protection from PTX's cytotoxicity, i.e., the reduction in viability for PTX and DFMO+PTX is similar. Normalized GR profiles of WT and DR cells under 6 h (A) 5-FU (8 μg/mL) and (B) PTX (8 μg/mL) treatments combined with DFMO (0.6 mM). Boxes represent the interquartile range, and white squares are the average value of GR data. The number of MCF-7 cells used in the growth profile calculations is 50. Control/DMSO: orange, DFMO: black, 5-FU: green, PTX: blue, DFMO+5-FU: red, DFMO+PTX: magenta.

also shows that the treated cells could be better discriminated with the control group for higher concentrations, and AUC converges to 1 at 10 μg/mL PXT (Figure 4D, inset). Similarly, PTX was diluted with DMSO, e.g., normalized GR and ROC analysis did not show any variations in the growth profile due to DMSO.

Viability study also demonstrates the susceptibility of MCF-7 cells to both 5-FU (Figure 4C) and PTX (Figure 4F) treatments. As observed in the GR measurements, the reduction in viability due to 5-FU is greater than PTX. Our observations in this section demonstrate the capability of our plasmonic functional assay platform to determine cell response to two single-drug therapies, where GR profiling precedes loss of cell viability, e.g., a meaningful drop in the cell viability was observed at $t = 18$ h for 5-FU and $t = 24$ h for PTX.

Functional Assay Platform Determines the Effect of DFMO on 5-FU and PTX Therapies. 5-FU could be used as a single agent,[43] while its response rates were found much higher when combined with other drug options.[44] As shown in the literature, DFMO increases the cell's sensitivity to 5-FU.[45,46] Figure 5A shows the GR profile of WT and DR cells exposed to 5-FU (8 μg/mL) combined with DFMO (0.6 mM) for 6 h treatment duration. In all treatment groups, WT cells exhibit a significant reduction in their GR profile compared to control. The mean normalized GR value calculated for control (0.1851) (for DMSO, mean normalized GR = 0.1851) reduced

to 0.0117 for DFMO and −0.0476 for 5-FU. More importantly, the reduction in GR is more pronounced for 5FU − DFMO combination compared to the single agent treatments (Figure 5, Scenario [i]), e.g., mean normalized GR for DFMO + 5-FU is −0.1501. Welch's t-test also shows a further reduction in GR profile for drug combination compared to the single-drug therapies, e.g., p(DMSO) = 0.9244, p(DFMO) = 4.3023×10^{-31}, p(5-FU) = 8.4673×10^{-39} and p(DFMO+5-FU) = 1.2892e-55 × 10^{-59}. In contrast, no additional reduction in GR was observed following the addition of DFMO to 5-FU for DR cells due to their resistant character to DFMO exposure (Figure 5, Scenario [ii]). For example, the normalized GR values were determined as 0.1842 (control), 0.1894 (DMSO), 0.1832 (DFMO), −0.0452, (5-FU), and −0.0494 (DFMO+5-FU). Welch's t-test also demonstrates that the GR profile of DR cells reduced only upon treatments containing 5-FU, e.g., p(DMSO) = 0.5759, p(DFMO) = 0.9179, p(5-FU) = 1.2180×10^{-40} and p(DFMO +5-FU) = 1.0364×10^{-38}.

More interestingly, DFMO triggers an opposite effect on PTX therapy. Polyamine levels are inhibited in DFMO-treated cells, which reverses the cytotoxicity of PTX. Therefore, treatment of WT cells with DFMO, which depletes the polyamine levels, protects cells from the cytotoxicity caused by PTX (Figure 5, Scenario [iii]).[47] Figure 5B shows the GR profile of WT and DR cells exposed to PTX (8 μg/mL)
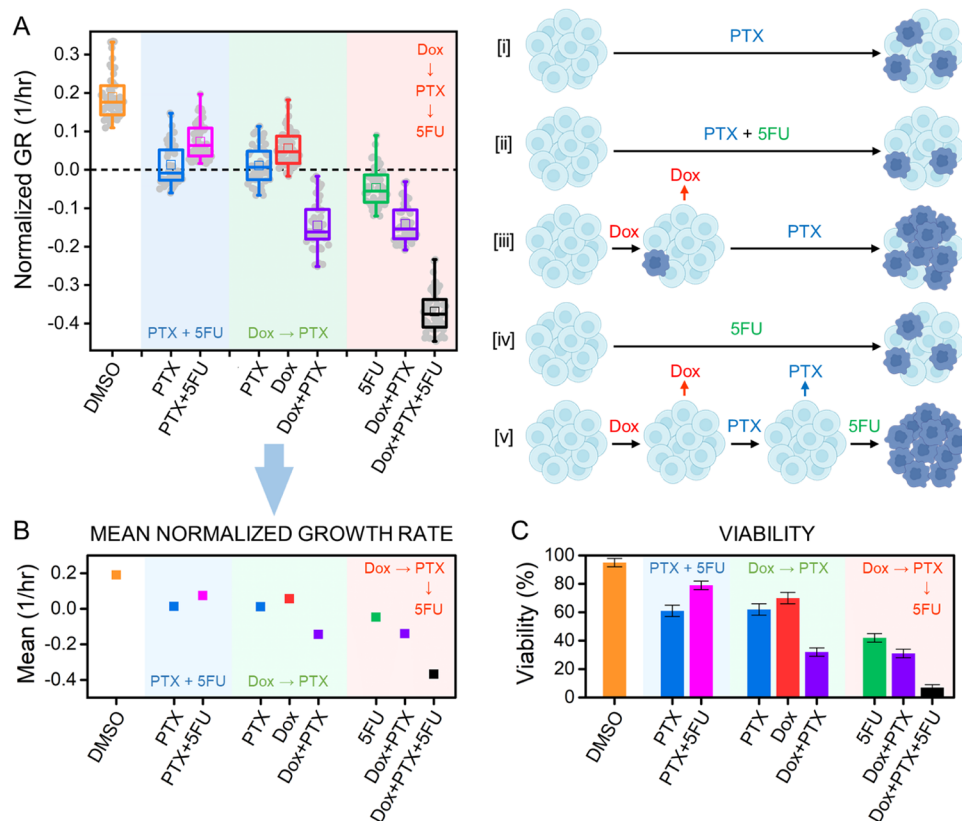
Figure 6. Plasmonic platform defines response to drug combinations. Schematics illustrates five cases: WT cells are sensitive to PTX and simultaneous exposure to PTX and 5-FU decreases PTX efficiency, i.e., [i] reduction in viability for PTX is higher compared to [ii] PTX+5-FU. WT cells are sensitive to Dox, e.g., viability reduces with single Dox therapy. Pretreatment with Dox increases the activity of PTX, i.e., [iii] reduction in viability for Dox → PTX sequence is much higher compared to [i] single PTX therapy. WT cells are sensitive to 5-FU and Dox → PTX sequence before 5-FU treatment (a washout step applied before 5-FU) increases 5-FU's efficiency, i.e., [v] reduction in viability for Dox → PTX → 5-FU is much higher compared to [iv] single 5-FU therapy. (A) Normalized GR profile, (B) mean normalized GR values, and (C) viability of WT cells under DMSO (orange), PTX (blue), 5-FU (green), Dox (red), PTX+5-FU (magenta), Dox → PTX sequence (violet), and Dox → PTX → 5-FU sequence (black). In the normalized GR profiles, boxes represent the interquartile range and white squares are the average value of GR data. The number of MCF-7 cells used in the growth profile calculations is 50. For viability tests, squares are the mean values and the error bars are double the standard deviation of five independent experiments.

combined with DFMO (0.6 mM) for 6 h treatment duration. Mean normalized GR value calculated for control, e.g., 0.1811 (For DMSO, mean normalized GR = 0.1872) reduced to 0.0090 for DFMO and 0.0161 for PTX. On the other hand, inhibiting PTX's cytotoxic effect via DFMO, mean normalized GR was found greater than those calculated for single-drug therapies, e.g., 0.1399 (DFMO+PXT). Welch's t-test also exhibits DFMO's reversing effect on PTX's cytotoxicity, e.g., p(DMSO) = 0.4216, p(DFMO) = 1.6231 × 10^{-31}, p(PTX) = 1.6629 × 10^{-29} and p(DFMO+PTX) = 1.0245 × 10^{-4}. In contrast, for DR cells, high ODC activity, in other words, high intracellular polyamine content, results in the reversal of the protection from PTX's cytotoxic effects (Figure 5, Scenario [iv]).[47] For DR cells, mean normalized GR values are similar for control and DFMO, e.g., 0.1804 (control), 0.1872 (DMSO), and 0.1891 (DFMO). Due to the sensitivity to PTX therapy, normalized GR dropped to 0.0195. On the other hand, DFMO's protection from PTX is not valid due to the resistance to the depletion of polyamine levels, i.e., the normalized GR value for DFMO+PTX is similar (0.0183) to PTX. Welch's t-test also shows a similar trend, e.g., p-values were calculated as p(DMSO) = 0.3890, p(DFMO) = 0.3390, p(PTX) = 1.0233 × 10^{-33} and p(DFMO+PTX) = 2.0433 × 10^{-30}. These results show that our technique could precisely

identify how the effect of a drug molecule is altered in combination drug therapies.

Plasmonic Platform Reveals Response to Combination Therapy. In order to validate the ability of our platform to define therapeutic response to combinations of SOC agents, we explored the growth profile of MCF-7 cells under a wide range of drug combinations. In addition to 5-FU and PTX, we studied a chemotherapy drug, e.g., doxorubicin (Dox) that could slow or stop cancer cell growth by blocking topoisomerase II enzyme and by the generation of free radicals.[48] Figure 6A,B shows the normalized GR profile for different combinations of 5-FU, PTX, and Dox (box plots), and the mean of each data set (dots), respectively. Figure 6C shows the viability study associated with the therapies of the same drug combinations. We first investigated the synergistic effect of 5-FU (8 μg/mL) and PTX (8 μg/mL) for 6 h treatment duration. As shown in the literature, simultaneous exposure of the two drugs or 5-FU pretreatment could reduce cell death compared to single PTX therapy (Figure 6, Scenario [i] vs [ii]).[49] For instance, the mean normalized GR calculated for DMSO (orange dot: 0.1897) decreases more for PTX (blue dot: 0.0132) compared to PTX − 5-FU combination (magenta dot: 0.0735). Welch's t-test, comparing cells under DMSO and the drug-treated cells, also exhibits the reduction in PTX's

efficiency when combined with 5-FU, e.g., p(PTX) = 1.5507 × 10^{-28} and p(PTX+5FU) = 1.3124 × 10^{-18}. Viability study, where MCF-7 cells were exposed to single PTX therapy and PTX − 5-FU combination for 48 h, reveals similar trends in the therapeutic profiles, e.g., PTX's antigrowth effect decreases in combination drug therapy (orange/blue/magenta bars: DMSO/PTX/PTX+5-FU).

More importantly, as shown in the literature, a short Dox pretreatment could enhance the activity of PTX (Figure 6, Scenario [i] vs [iii]).[50] For instance, treating MCF-7 cells with 1 μg/mL Dox for 2 h decreases the mean normalized GR to 0.0562 (red dot). After Dox exposure, the medium with drug was removed, and the cells were treated with PTX for 6 h. The mean normalized GR calculated for PTX (blue dot: 0.0112) dramatically decreases to negative values for the Dox → PTX sequence (violet dot: −0.1447). Welch's t-test also shows this strong reduction in GR profile due to Dox pretreatment, e.g., p(PTX) = 1.1619 × 10^{-29}, p(Dox) = 2.9741 × 10^{-22} and p(Dox → PTX) = 1.2914 × 10^{-47}. Viability study for 48 h of single-drug therapies demonstrates the antitumor effect of PTX (blue bar) and Dox (red bar). 48 h PTX exposure following pretreatment with Dox for 6 h (violet bar) reduces viability much stronger compared to 48 h single PTX therapy (blue bar).

As shown in the literature, Dox → PTX pretreatment reduces basal thymidylate synthase expression, which increases 5-FU activity (Figure 6, Scenario [iv] vs Scenario [v]).[51] After Dox → PTX sequence (2 h Dox and 6 h PTX pretreatment), the medium was replaced with a drug-free medium, where MCF-7 cells were cultured for 12 h. Later, the drug-free medium was replaced with 5-FU medium, where the treatment duration was 6 h. The mean normalized GR values for 5-FU and Dox → PTX sequence were calculated as −0.0471 (green dot) and −0.1407 (violet dot), respectively (for DMSO, 0.1897). The reduction in GR profile was dramatically pronounced due to the synergistic effect between 5-FU and Dox → PTX sequence, i.e., the mean normalized GR was calculated as −0.3687 (black dot). Welch's t-test, comparing cells under DMSO with the drug-treated cells, also exhibits the synergistic effect of the three-drug combination, e.g., p(5-FU) = 3.7502 × 10^{-39}, p(Dox → PTX) = 1.0884 × 10^{-51}, and p(Dox → PTX → 5-FU) = 2.3505 × 10^{-71}. Viability study also demonstrates the strengthening effect of Dox → PTX sequence on the activity of 5-FU treatment. Here, cells were treated with Dox for 6 h prior to PTX treatment for 48 h. Then, cells were treated with 5-FU for 48 h following a resting period of 48 h in a drug-free medium. The data also demonstrates that for 5-FU treatment after Dox → PTX sequence (black bar), the reduction in viability is pronounced dramatically compared to 5-FU (green bar) and Dox → PTX sequence (violet bar). These results confirm our technology's ability to identify the response of cancer cells to drug combinations as well as determine additive and antagonistic effects between drugs in combined therapies.

Future Perspective. Our data revealing the effect of single-drug therapies, and synergic or antagonistic effect of drug combinations demonstrate the potential of our plasmonic functional assay platform to determine personalized drug therapies for cancer patients. One option from many therapeutic selections is used in the clinical decision based on multiple parameters related to patients. Here, our plasmonic functional assay platform could help physicians to precisely determine the therapeutic strategy by adding a critical

parameter. Using patients' own cells that could be obtained by biopsy, and evaluating their response to a variety of available antitumor agents, our plasmonic platform could be used for both induction therapy and post-relapse treatment. Based on the diagnosis, patients undergo induction therapy, where our platform could increase the success of finding the therapeutic agents from many options that leads to complete response. In general, induction therapy is followed by consolidation therapy to kill cancer cells that may be left in the body after the cancer disappears. Maintenance therapy is then followed to keep cancer from relapse. However, there is still a high potential for relapse. In the presence of relapse, clinical decision is made based on the prior therapies received and the physician's clinical experience. In this particular case, our technology could help physicians to determine the optimum drug therapy from the remaining treatment options.

CONCLUSIONS

In conclusion, we introduced a high-throughput and sensitive plasmonic functional assay platform to identify the therapeutic profile of cancer cells in single-cell precision. Our platform could determine the growth profile of populations by assessing the mass and mass accumulation rate of individual cells. Using this ability, the technology could identify the biophysical properties of cells, and determine the therapeutic effects of cancer drugs by monitoring the variations within these properties through ex vivo measurements. Using our platform, we could monitor cells with a scanning rate of > ∼500 cells/h to determine the growth profile of populations. Thus, our technique brings a new modality to assess the therapeutic profile of cancer cells much faster compared to cell culture-based classical methods. We could determine the therapeutic profile of cancer cells by using the changes observed within their growth profile under certain drugs or their combinations. The platform could identify the resistant behavior of subpopulations to different drug treatments, revealing their therapeutic heterogeneity, which is a critical advantage over bulk analyses as we could provide therapeutic profiles in single-cell precision. For a proof-of-principle demonstration of our technology, we used MCF-7 cells and studied the therapeutic effects of standard-of-care (SOC) drugs, e.g., difluoromethylornithine (DFMO), 5-fluorouracil (5-FU), paclitaxel (PTX), and doxorubicin (Dox). Using our platform, we successfully demonstrated the antitumor effects of therapies utilizing single SOC agents or their combinations. We also investigated the effect of drug order in the combination therapies on the overall antitumor effect. Providing accurate information related to drug susceptibility, functional assay platforms could be strong candidates for clinical applications, while they are limited by bulk measurement approaches and long-term cell cultures. Eliminating these requirements by precisely providing therapeutic information with small sample volumes, our single-cell plasmonic functional assay platform could transform approaches relying on functional assays to a technology identifying personalized drug therapies.

EXPERIMENTAL SECTION

Fabrication of the Plasmonic Chips. All fabrication steps were performed on a 100 nm LPCVD silicon nitrite coated 4-in wafer (LPCVD = low-pressure chemical vapor deposition). The silicon nitride surface was coated with a 120 nm thick aluminum film, while 5 nm thick titanium film was used as an adhesion layer. The aluminum surface was coated with a photoresist, and deep ultraviolet lithography

was performed to define apertures throughout the resist. Following the development of the photoresist, the aluminum film was etched with ion milling, realizing periodic nanohole arrays. The remaining photoresist was removed from the metal surface with oxygen plasma, and the aluminum surface was coated with 2 nm silicon dioxide. Finally, the wafer was diced to realize plasmonic chips with the desired dimensions. This fabrication technique ensures high-quality periodic apertures that are uniformly distributed over large areas.

Preparation of the Cell Culture. For growth rate measurements, we used MCF-7 cells (ATCC HTB-22). The cells were maintained in RPMI 1640 medium supplemented with 10% FBS, 10% penicillin, and 1% nonessential amino acids in a humidified Thermo Scientific Forma 371 incubator at 37 °C and 5% CO_2.

Spectrometer-Based Functional Assay Platform. In the spectral measurements, we used a microscope (Zeiss Axio), where we fiber-coupled a multichannel spectrometer system using achromatic and objective lenses, and a fiber collimator. Plasmonic chips were illuminated with a broadband white LED source, and the transmitted light from the chips was collected with an objective lens. For spectral measurements, we used two multichannel spectrometer systems, where the visible frequency range was divided with five and three simultaneously performing spectrometers with 5 μm slit width. Dividing the spectral range of interest with multiple spectrometers, we could achieve better spectral resolution, e.g., the spectrometer system of five spectrometers (Avantes B.V. with multifurcated fiber cable) has a spectral resolution of 0.09 nm, while the one with three spectrometers (Ocean Insight with trifurcated fiber cable) has 0.15 nm spectral resolution.[26] Considering the minute mass changes in sub-1 pg/hr level, which yields small variations within the transmission response of the nanohole arrays, optical setups were located on a vibration isolator. In the light-coupling scheme, we utilized a motorized translation stage to precisely couple the transmitted light from the plasmonic chip to the spectrometer systems. The microscope stage was encapsulated with a PeCon cell culture incubator, and the incubator parameters were maintained with a Zeiss incubation control platform at 5% CO_2, 37.0 °C, and 95% humidity.

Spectral Postprocessing Technique. The raw spectrometer data was smoothed with a Savitzky–Golay filter. The biomass variations on the plasmonic chip surface for a 10-minute-long growth rate measurement are small, e.g., ~pg/hr level. These mass variations create small refractive index changes, which result in spectral shifts below 1 nm.[26] Therefore, monitoring spectral shifts within the plasmonic resonances (e.g., transmission maxima in our case) could be insufficient to determine the rate of mass change. To address this problem, we utilized a postprocessing technique that could consider the collective spectral variations within the plasmonic resonances. Recently, we used such a technique to detect protein concentrations in sub-1 ng/mL level,[29,31] and to determine the growth profile of populations in single-cell precision.[26] To consider the collective spectral shifts, we calculated the integral of the transmission curve within a 60 nm wide spectral window, positioned to close proximity of the transmission resonance, where the largest spectral shifts occur as a result of strong light–matter interactions. Considering the transmission resonance with a Lorentzian shape, we positioned the spectral window ensuring that the transmission maximum always positions at wavelengths shorter than the spectral window during the growth-profiling tests. This methodology eliminates the effect of Lorentzian shape of the transmission resonance on the growth rate calculations.[30] Accumulated mass (mass loss) on the sensor surface shifts the transmission resonance toward longer (shorter) wavelengths, i.e., it overlaps better (worse) with the spectral window, which increases (decreases) the SI value. For example, Figure 2I demonstrates the consistent increase in SI due to the accumulated cellular mass.

Preparation of DR Cells. Wild-type MCF-7 cells were exposed to different DFMO concentrations, e.g., in the order of 0.1, 0.2, 0.4, 0.6, and 0.8 mM for 4 weeks (total 20 weeks). At the end of each concentration treatment, growth profiles of treated DR cells were compared to those of untreated WT cells. The similar growth profile between the treated DR cells and the untreated WT cells for each concentration reveals the resistant nature of DR cells to such DFMO

concentration. DR cells prepared with this protocol could adapt to DFMO concentrations up to 0.8 mM.

■ AUTHOR INFORMATION

Corresponding Author

Arif E. Cetin − *Izmir Biomedicine and Genome Center, Balcova 35330 Izmir, Turkey;* orcid.org/0000-0002-0788-8108; Email: arifengin.cetin@ibg.edu.tr

Authors

Seda Nur Topkaya − *Department of Analytical Chemistry, Faculty of Pharmacy, Izmir Katip Celebi University, Cigli 35620 Izmir, Turkey*

Ziya Ata Yazici − *Department of Computer Engineering, Faculty of Computer and Informatics Engineering, Istanbul Technical University, 34467 Istanbul, Turkey;* orcid.org/0000-0001-7051-833X

Ozden Yalcin-Ozuysal − *Department of Molecular Biology and Genetics, Izmir Institute of Technology, Urla 35430 Izmir, Turkey;* orcid.org/0000-0003-0552-368X

Complete contact information is available at:
https://pubs.acs.org/10.1021/acssensors.3c00208

Notes

The authors declare the following competing financial interest(s): A.E.C. has a granted patent (PCT/TR2021/051179, TR2020/19537) for the presented growth-profiling platform.

■ REFERENCES

(1) Krzyszczyk, P.; Acevedo, A.; Davidoff, E. J.; Timmins, L. M.; Marrero-Berrios, I.; Patel, M.; White, C.; Lowe, C.; Sherba, J. J.; Hartmanshenn, C.; et al. The Growing Role of Precision and Personalized Medicine for Cancer Treatment. *Technology* **2018**, *06*, 79–100.

(2) Wei, Y.; Xia, H.; Zhang, F.; Wang, K.; Luo, P.; Wu, Y.; Liu, S. Theranostic Nanoprobe Mediated Simultaneous Monitoring and Inhibition of P-Glycoprotein Potentiating Multidrug-Resistant Cancer Therapy. *Anal. Chem.* **2019**, *91*, 11200–11208.

(3) Wu, Y.; Zhang, F.; Wang, K.; Luo, P.; Wei, Y.; Liu, S. Activatable Fluorescence Imaging and Targeted Drug Delivery via Extracellular Vesicle-Like Porous Coordination Polymer Nanoparticles. *Anal. Chem.* **2019**, *91*, 14036–14042.

(4) Wu, Y.; Gao, Y.; Su, J.; Chen, Z.; Liu, S. In Situ Detection of Intracellular Tissue Transglutaminase Based on Aggregation-Induced Emission. *Chem. Commun.* **2020**, *56*, 9008–9011.

(5) Wu, Y.; Chen, Z.; Yao, Z.; Zhao, K.; Shao, F.; Su, J.; Liu, S. Black Phosphorus Quantum Dots Encapsulated Biodegradable Hollow Mesoporous MnO 2: Dual-Modality Cancer Imaging and Synergistic Chemo-Phototherapy. *Adv. Funct. Mater.* **2021**, *31*, No. 2104643.

(6) Housman, G.; Byler, S.; Heerboth, S.; Lapinska, K.; Longacre, M.; Snyder, N.; Sarkar, S. Drug Resistance in Cancer: An Overview. *Cancers* **2014**, *6*, 1769–1792.

(7) Vasan, N.; Baselga, J.; Hyman, D. M. A View on Drug Resistance in Cancer. *Nature* **2019**, *575*, 299–309.

(8) Konieczkowski, D. J.; Johannessen, C. M.; Garraway, L. A. A Convergence-Based Framework for Cancer Drug Resistance. *Cancer Cell* **2018**, *33*, 801−815.

(9) McGranahan, N.; Swanton, C. Clonal Heterogeneity and Tumor Evolution: Past, Present, and the Future. *Cell* **2017**, *168*, 613−628.

(10) Dimopoulos, M. A.; Terpos, E.; Niesvizky, R.; Palumbo, A. Clinical Characteristics of Patients with Relapsed Multiple Myeloma Q. *Cancer Treat. Rev.* **2015**, *41*, 827−835.

(11) Belkacemi, Y.; Hanna, N. E.; Besnard, C.; Majdoul, S.; Gligorov, J. Local and Regional Breast Cancer Recurrences: Salvage Therapy Options in the New Era of Molecular Subtypes. *Front. Oncol.* **2018**, *8*, No. 112.

(12) Ushijima, K. Treatment for Recurrent Ovarian Cancer - At First Relapse. *J. Oncol.* **2010**, *2010*, No. 497429.

(13) Mellinghoff, I. K.; Wang, M. Y.; Vivanco, I.; Haas-Kogan, D. A.; Zhu, S.; Dia, E. Q.; Lu, K. V.; Yoshimoto, K.; Huang, J. H. Y.; Chute, D. J.; et al. Molecular Determinants of the Response of Glioblastomas to EGFR Kinase Inhibitors. *N. Engl. J. Med.* **2005**, *353*, 2012−2024.

(14) Garraway, L. A.; Jänne, P. A. Circumventing Cancer Drug Resistance in the Era of Personalized Medicine. *Cancer Discovery* **2012**, *2*, 214−226.

(15) Navin, N.; Kendall, J.; Troge, J.; Andrews, P.; Rodgers, L.; McIndoo, J.; Cook, K.; Stepansky, A.; Levy, D.; Esposito, D.; et al. Tumour Evolution Inferred by Single-Cell Sequencing. *Nature* **2011**, *472*, 90−95.

(16) Stevens, M. M.; Maire, C. L.; Chou, N.; Murakami, M. A.; Knoff, D. S.; Kikuchi, Y.; Kimmerling, R. J.; Liu, H.; Haidar, S.; Calistri, N. L.; et al. Drug Sensitivity of Single Cancer Cells Is Predicted by Changes in Mass Accumulation Rate. *Nat. Biotechnol.* **2016**, *34*, 1161−1167.

(17) Cetin, A. E.; Stevens, M. M.; Calistri, N. L.; Fulciniti, M.; Olcum, S.; Kimmerling, R. J.; Munshi, N. C.; Manalis, S. R. Determining Therapeutic Susceptibility in Multiple Myeloma by Single-Cell Mass Accumulation. *Nat. Commun.* **2017**, *8*, No. 1613.

(18) Nath, A.; Bild, A. H. Leveraging Single-Cell Approaches in Cancer Precision Medicine. *Trends Cancer* **2021**, *7*, 359−372.

(19) Brady, S. W.; McQuerry, J. A.; Qiao, Y.; Piccolo, S. R.; Shrestha, G.; Jenkins, D. F.; Layer, R. M.; Pedersen, B. S.; Miller, R. H.; Esch, A.; et al. Combating Subclonal Evolution of Resistant Cancer Phenotypes. *Nat. Commun.* **2017**, *8*, No. 1231.

(20) Francis, J. M.; Zhang, C. Z.; Maire, C. L.; Jung, J.; Manzo, V. E.; Adalsteinsson, V. A.; Homer, H.; Haidar, S.; Blumenstiel, B.; Pedamallu, C. S.; et al. EGFR Variant Heterogeneity in Glioblastoma Resolved through Single-Nucleus Sequencing. *Cancer Discovery* **2014**, *4*, 956−971.

(21) Friedman, A. A.; Letai, A.; Fisher, D. E.; Flaherty, K. T. Precision Medicine for Cancer with Next-Generation Functional Diagnostics. *Nat. Rev. Cancer* **2015**, *15*, 747−756.

(22) Montero, J.; Sarosiek, K. A.; Deangelo, J. D.; Maertens, O.; Ryan, J.; Ercan, D.; Piao, H.; Horowitz, N. S.; Berkowitz, R. S.; Matulonis, U.; et al. Drug-Induced Death Signaling Strategy Rapidly Predicts Cancer Response to Chemotherapy. *Cell* **2015**, *160*, 977−989.

(23) Wu, S.; Liu, X.; Zhou, X.; Liang, X. M.; Gao, D.; Liu, H.; Zhao, G.; Zhang, Q.; Wu, X. Quantification of Cell Viability and Rapid Screening Anti-Cancer Drug Utilizing Nanomechanical Fluctuation. *Biosens. Bioelectron.* **2016**, *77*, 164−173.

(24) Ferrezuelo, F.; Colomina, N.; Palmisano, A.; Gari, E.; Gallego, C.; Csikasz-Nagy, A.; Aldea, M. The Critical Size Is Set at a Single-Cell Level by Growth Rate to Attain Homeostasis and Adaptation. *Nat. Commun.* **2012**, *3*, No. 1012.

(25) Zangle, T. A.; Teitell, M. A. Live-Cell Mass Profiling: An Emerging Approach in Quantitative Biophysics. *Nat. Methods* **2014**, *11*, 1221−1228.

(26) Cetin, A. E.; Topkaya, S. N.; Yalcin-Ozuysal, O.; Khademhosseini, A. Refractive Index Sensing for Measuring Single Cell Growth. *ACS Nano* **2021**, *15*, 10710−10721.

(27) Barnes, W. L. Surface Plasmon-Polariton Length Scales: A Route to Sub-Wavelength Optics. *J. Opt. A Pure Appl. Opt.* **2006**, *8*, No. S87.

(28) Cetin, A. E.; Topkaya, S. N. Plasmonic Diffraction Field Pattern Imaging Could Resolve Ultrasensitive Bioinformation. *ACS Photonics* **2019**, *6*, 2626−2635.

(29) Cetin, A. E.; Etezadi, D.; Galarreta, B. C.; Busson, M. P.; Eksioglu, Y.; Altug, H. Plasmonic Nanohole Arrays on a Robust Hybrid Substrate for Highly Sensitive Label-Free Biosensing. *ACS Photonics* **2015**, *2*, 1167−1174.

(30) Yanik, A. A.; Cetin, A. E.; Huang, M.; Artar, A.; Mousavi, S. H.; Khanikaev, A.; Connor, J. H.; Shvets, G.; Altug, H. Seeing Protein Monolayers with Naked Eye through Plasmonic Fano Resonances. *Proc. Natl. Acad. Sci. U.S.A.* **2011**, *108*, 11784−11789.

(31) Cetin, A. E.; Topkaya, S. N. Photonic Crystal and Plasmonic Nanohole Based Label-Free Biodetection. *Biosens. Bioelectron.* **2019**, *132*, 196−202.

(32) Son, S.; Tzur, A.; Weng, Y.; Jorgensen, P.; Kim, J.; Kirschner, M. W.; Manalis, S. R. Direct Observation of Mammalian Cell Growth and Size Regulation. *Nat. Methods* **2012**, *9*, 910−912.

(33) Otsu, N. A Threshold Selection Method from Gray-Level Histograms. *IEEE Trans. Syst. Man. Cybern.* **1979**, *9*, 62−66.

(34) Alexiou, G. A.; Lianos, G. D.; Ragos, V.; Galani, V.; Kyritsis, A. P. Difluoromethylornithine in Cancer: New Advances. *Futur. Oncol.* **2017**, *13*, 809−819.

(35) Casero, R. A.; Pegg, A. E. Polyamine Catabolism and Disease. *Biochem. J.* **2009**, *421*, 323−338.

(36) Canizares, F.; Salinas, J.; De Las Heras, M.; Diaz, J.; Tovar, I.; Martinez, P.; Penafiel, R. Prognostic Value of Ornithine Decarboxylase and Polyamines in Human Breast Cancer: Correlation with Clinicopathologic Parameters. *Clin. Cancer Res.* **1999**, *5*, 2035−2041.

(37) Kremmer, T.; Palyi, I.; Daubner, D.; Boldizsar, M.; Vincze, B.; Paulik, E.; Sugar, J.; Pokorny, E.; Tury, E. Comparative Studies on the Polyamine Metabolism and DFMO Treatment of MCF-7 and MDA-MB-231 Breast Cancer Cell Lines and Xenografts. *Anticancer Res.* **1991**, *11*, 1807−1813.

(38) McCann, P. P.; Pegg, A. E. Ornithine Decarboxylase as an Enzyme Target for Therapy. *Pharmacol. Ther.* **1992**, *54*, 195−215.

(39) Das, B.; Vig, M.; Khurana, K. K.; Madhubala, R. Isolation and Characterization of Human Breast Adenocarcinoma Cells Made Resistant to α-Difluoromethylornithine. *Cancer Invest.* **2000**, *18*, 115−122.

(40) Pencina, M. J.; D'Agostino, R. B.; D'Agostino, R. B.; Vasan, R. S. Evaluating the Added Predictive Ability of a New Marker: From Area under the ROC Curve to Reclassification and Beyond. *Stat. Med.* **2008**, *27*, 157−172.

(41) Curreri, A. R.; Ansfield, F. J.; Mclver, F. A.; Waisman, H. A.; Heidelberger, C. Clinical Studies with 5-Fluorouracil. *Cancer Res.* **1958**, *18*, 478−484.

(42) Patt, D.; Gauthier, M.; Giordano, S. Paclitaxel in Breast Cancer. *Women's Heal.* **2006**, *2*, 11−21.

(43) Ansfield, F. J.; Ramirez, G.; Mackman, S.; Bryan, G. T.; Curreri, A. R. A Ten-Year Study of 5-Fluorouracil in Disseminated Breast Cancer with Clinical Results and Survival Times. *Cancer Res.* **1969**, *29*, 1062−1066.

(44) Jones, R. B.; Shpall, E. J.; Shogan, J.; Affronti, M.; Lou; Coniglio, D.; Hart, L.; Halperin, E.; Dirk Iglehart, J.; Moore, J.; Gockerman, J.; et al. The Duke Afm Program Intensive Induction Chemotherapy for Metastatic Breast Cancer. *Cancer* **1990**, *66*, 431−436.

(45) Kingsnorth, A. N.; Russell, W. E.; McCann, P. P.; Diekema, K. A.; Malt, R. A.; Kingsnorth, A. N.; Russell, W. E.; McCann, P. P.; Diekema, K. A.; Malt, R. A.; et al. Effects of α-Difluoromethylornithine and 5-Fluorouracil on the Proliferation of a Human Colon Adenocarcinoma Cell Line. *Cancer Res.* **1983**, *43*, 4035−4038.

(46) Barranco, S. C.; Townsend, C. M.; Ho, B. Y.; Reumont, K. J.; Koester, S. K.; Ford, P. J. Schedule Dependent Potentiation of Antitumor Drug Effects by α-Difluoromethylornithine in Human Gastric Carcinoma Cells in Vitro. *Invest. New Drugs* **1990**, *8*, S9−S18.

(47) Das, B.; Rao, A. R.; Madhubala, R. Difluoromethylornithine Antagonizes Taxol Cytotoxicity in MCF-7 Human Breast Cancer Cells. *Oncol. Res.* **1997**, *9*, 565−572.

(48) Tacar, O.; Sriamornsak, P.; Dass, C. R. Doxorubicin: An Update on Anticancer Molecular Action, Toxicity and Novel Drug Delivery Systems. *J. Pharm. Pharmacol.* **2012**, *65*, 157−170.

(49) Kano, Y.; Akutsu, M.; Tsunoda, S.; Ando, J.; Matsui, J.; Suzuki, K.; Ikeda, T.; Inoue, Y.; Adachi, K. Schedule-Dependent Interaction between Paclitaxel and 5-Fluorouracil in Human Carcinoma Cell Lines in Vitro. *Br. J. Cancer* **1996**, *74*, 704−710.

(50) Zoli, W.; Ricotti, L.; Barzanti, F.; Dal Susino, M.; Frassineti, G. L.; Milandri, C.; Casadei Giunchi, D.; Amadori, D. Schedule-Dependent Interaction of Doxorubicin, Paclitaxel and Gemcitabine in Human Breast Cancer Cell Lines. *Int. J. Cancer* **1999**, *80*, 413−416.

(51) Zoli, W.; Ulivi, P.; Tesei, A.; Fabbri, F.; Rosetti, M.; Maltoni, R.; Giunchi, D. C.; Ricotti, L.; Brigliadori, G.; Vannini, I.; Amadori, D. Addition of 5-Fluorouracil to Doxorubicin-Paclitaxel Sequence Increases Caspase-Dependent Apoptosis in Breast Cancer Cell Lines. *Breast Cancer Res.* **2005**, *7*, No. R681.

M